



HAL
open science

Experimental characterization and numerical modeling of crack initiation in rhombus hole PMMA specimens under compression

Aurélien Doitrand, Rafael Estevez, Dominique Leguillon

► **To cite this version:**

Aurélien Doitrand, Rafael Estevez, Dominique Leguillon. Experimental characterization and numerical modeling of crack initiation in rhombus hole PMMA specimens under compression. *European Journal of Mechanics - A/Solids*, 2019, 76, pp.290-299. 10.1016/j.euromechsol.2019.04.013 . hal-02302541

HAL Id: hal-02302541

<https://hal.science/hal-02302541>

Submitted on 1 Oct 2019

HAL is a multi-disciplinary open access archive for the deposit and dissemination of scientific research documents, whether they are published or not. The documents may come from teaching and research institutions in France or abroad, or from public or private research centers.

L'archive ouverte pluridisciplinaire **HAL**, est destinée au dépôt et à la diffusion de documents scientifiques de niveau recherche, publiés ou non, émanant des établissements d'enseignement et de recherche français ou étrangers, des laboratoires publics ou privés.

Experimental characterization and numerical modeling of crack initiation in rhombus hole PMMA specimens under compression

Aurélien Doitrand^{1*}, Rafael, Estevez¹, Dominique Leguillon²

¹, *Université Grenoble-Alpes - CNRS UMR 5266, SIMaP, F-38000 Grenoble, France*

²*Institut Jean le Rond d'Alembert, Sorbonne Université, CNRS, UMR 7190, F-75005 Paris, France*

Abstract

Under compression, mode I cracking in the loading direction is observed in PMMA rhombus hole specimens. Except for specimens containing flaws, spontaneous initiation is observed experimentally with the instantaneous formation of a crack in undamaged specimens. With increasing hole angle and size, the initiation force decreases whereas the crack arrest length increases. Similar influences of size and angle are predicted numerically by 2D and 3D finite element modeling of crack initiation using the coupled criterion, which allows crack initiation surface, shape and loading level to be determined. Initiation force and crack length depend on the specimen geometry and on boundary conditions. Compared to the 3D case, 2D modeling provides similar estimates of the crack length in the specimen middle plane and overestimates the initiation force. The 3D crack shapes predicted numerically qualitatively look like the crack shapes observed experimentally. A reasonable agreement between numerical predictions and experimental measurements of initiation force and crack length is obtained.

Keywords: Crack initiation; Crack jump; Coupled criterion

1. Introduction

Crack nucleation in brittle materials can be studied in the framework of Finite Fracture Mechanics (FFM) [8, 25], which consists in considering finite rather than infinitesimal crack increments as in classical linear elastic fracture mechanics (LEFM). LEFM allows the propagation of an already existing crack to be studied but fails to predict its initiation. To overcome this difficulty, Leguillon [9] proposed to model crack nucleation by coupling

*corresponding author, aurelien.doitrand@grenoble-inp.fr

stress and energy criteria, assuming that a crack of finite size initiates spontaneously at a prescribed loading. This approach is based on the assumption that the material abruptly changes from an undamaged to a cracked configuration in very short time and loading increments, with no steady state between them. The Coupled Criterion (CC) has been successfully used in order to predict crack initiation in several materials such as composites [1, 2, 7, 17, 21, 29], ceramics [14, 16, 22], rocks [12], etc. It can also be applied for crack initiation prediction at interfaces [3, 4, 18, 19, 32] or V-notch configurations [10, 11, 15, 28]. A particular interest of the CC is the possibility to identify material fracture properties that can not easily be measured experimentally, such as, *e.g.*, the strength and toughness of some interfaces [3, 4, 13], or the intrinsic strength of ceramic materials [16]. Weißgraeber *et al.* [34] proposed an extensive review about the CC which has, until now, mainly been applied to 2D cases. More recent works about the CC deal with its use in a nonlinear framework [31, 33] and its application in 3D cases [3, 4, 5, 6, 13, 23, 24, 26].

The CC states that crack initiation requires both a stress and an energy conditions to be simultaneously fulfilled. Combining both conditions allows the determination of the crack initiation length (in 2D) or surface (in 3D) and loading level. Depending on the studied material and loading configuration, the crack initiation length predicted by the CC may also be an arrest length. This phenomenon corresponds to some configurations for which the energy criterion is dominant with respect to the stress criterion [1, 2, 35]. In most cases, however, crack initiation is followed by an unstable crack propagation (as *e.g.*, observed experimentally in Homalite under mixed mode loading by Pham and Ravi-Chandar [27]), which may even lead to the final failure of the specimen [4]. In both cases, the CC predicts that at a given loading (the initiation loading), a crack instantaneously nucleates over a finite length. Doitrand *et al.* [6] recently showed that this abrupt crack jump at initiation in a brittle material can also be captured numerically using cohesive zone models. Although confrontations between experimental and numerical imposed loading are usually provided in analysis involving the CC, few works includes comparison of the crack arrest lengths obtained numerically and experimentally. From an experimental point of view, capturing the crack arrest length is not a straightforward task since it requires to record the material state just after initiation. For some configurations, it cannot be provided because of the instable crack propagation just after initiation triggering the complete specimen failure.

It may also require the use of micro computed tomography in cases where the emerging crack length on the specimen edge is not representative of the crack length inside the material. Romani *et al.* [30] highlighted spontaneous crack initiation in open hole plaster specimens using digital image correlation to track the crack length on the specimen edge by noticing that the slope of the crack length as a function of the imposed loading curve was almost vertical. However, no comparison between numerical prediction and experimental measurement of crack length was given.

The objective of the present work is to evaluate the validity of one of the major assumptions made in the CC, namely the hypothesis of a sudden crack jump at initiation, by means of experimental characterization and numerical modeling of crack initiation in rhombus hole specimens under compression. Experiments on PMMA specimens with various rhombus hole size and angle are presented in Section 2. A recall of the coupled criterion is provided in Section 3. Crack initiation in rhombus hole specimens is modeled by Finite Element (FE) both in 2D and 3D in Section 4. The numerical prediction of crack initiation are compared to the experimental results in Section 5.

2. Experiments on PMMA rhombus hole specimens

The material under investigation is PMMA. A main advantage of this material is its transparency, which allows cracks inside the material to be optically detected. Several rectangular specimens, manufactured using laser cutting in order to obtain rhombus holes, were tested under compression on a 20 kN Zwick testing machine. The choice of compression test on rhombus hole specimens is motivated by the fact that it leads to a crack arrest after initiation, followed by a stable crack propagation when increasing the applied load. The specimen geometry is depicted in Fig 1a. Two specimens of each configurations have been tested. The 40 tested specimens length, width and thickness respectively are $l = 59.5 \pm 0.05 \text{mm}$, $w = 39.5 \pm 0.05 \text{mm}$ and $t = 9.5 \pm 0.05 \text{mm}$, including five different hole angles β and four different hole sizes (obtained by varying the vertical half-diagonal length $s \times \cos \frac{\beta}{2}$, s being the rhombus side length). The specimen dimensions are summarized in Table 1. The experimental set-up is shown on Fig 1b. Swivel platens were used in order to ensure an uniaxial imposed compression loading. The imposed displacement rate was 0.5mm/min, which is small enough to be as close as possible to an overall quasi-static

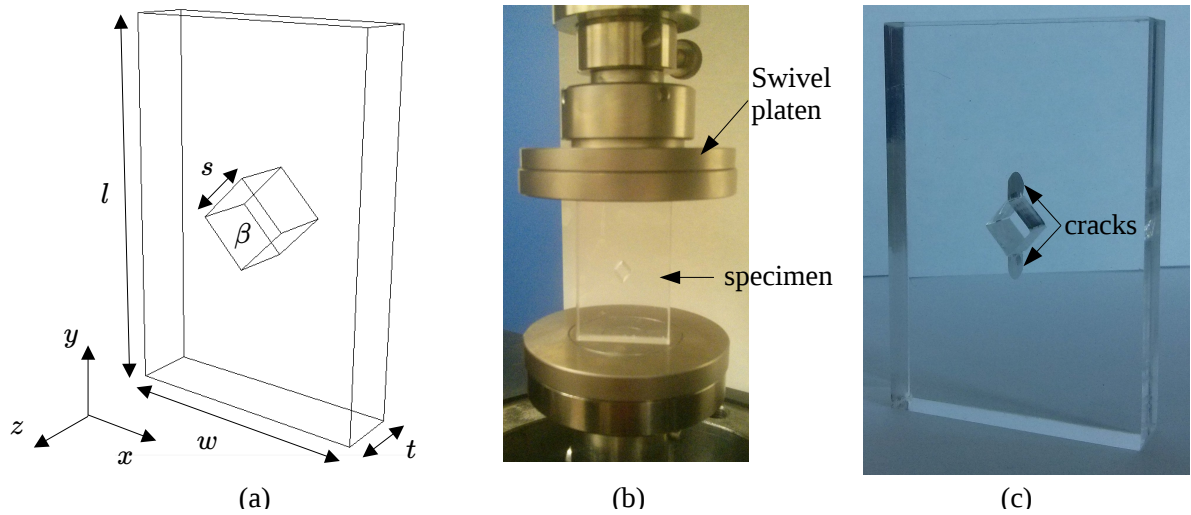


Figure 1: (a) Rhombus hole specimen dimensions, (b) experimental set-up of compression tests and (c) photograph of a cracked specimen.

loading state. Images of the specimen were acquired at 1 Hz frequency using a Allied Vision Prosilica GX camera, with a shutter speed of almost one second, which allows capturing a crack that initiates between two image acquisitions. The displacement increment between two recorded pictures is 8.3×10^{-3} mm, which ensures a crack length increment lower than 0.2 mm during the stable crack propagation phase. Therefore, the uncertainty on the measured crack length is at most 0.2 mm.

For each specimen under investigation, cracking occurs at the upper and lower rhombus V-notch in mode I. A vertical crack takes place in the direction of the compression loading. An example of a cracked specimen is shown in Fig. 1c. The crack length in the specimen middle plane have been measured manually from the 2D recorded cracked specimen images. The uncertainty about the crack measurement is estimated to be at most 0.1 mm. It is worth noting that some of the studied specimen contains flaws near the V-notch that might

Specimens	A	B	C	D	
$s \times \cos(\frac{\beta}{2})$ (mm)	7.4	6.4	5.3	4.2	
Specimens	1	2	3	4	5
β (deg.)	70	80	90	100	110

Table 1: Specimen dimensions: rhombus hole angle β and half-diagonal length ($s \times \cos(\frac{\beta}{2})$). For instance, specimen B3 contains a rhombus hole with 6.4 mm vertical half-diagonal and 90 deg. angle.

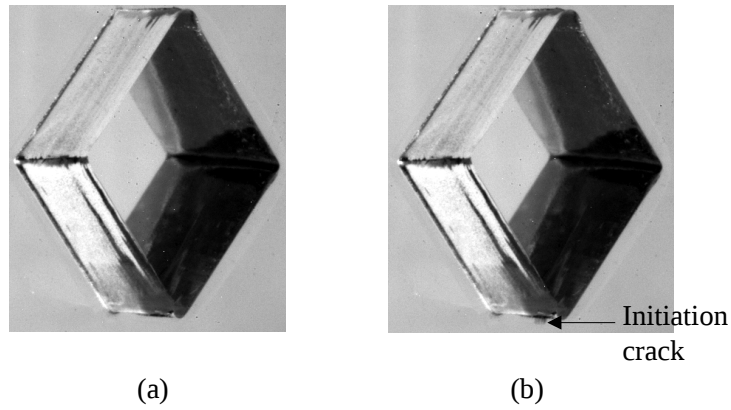


Figure 2: Focus on B1 specimen rhombus hole (6.4mm half-vertical diagonal, 70 deg. angle) (a) just before and (b) at crack initiation. The imposed displacement variation between both states is 8×10^{-3} mm.

have been created during specimen manufacturing. For those specimens, crack initiation occurs near a flaw (*cf.* Fig. 2), resulting in a rather progressive growth of the crack from this flaw. This is particularly observed for some specimens exhibiting the smallest angles ($\beta < 90$ deg.) However, for most of the specimens, spontaneous crack nucleation is observed in the undamaged specimens. As shown in Fig. 3, there is a sudden "jump" between a state with no crack (Fig. 3a) and a state with a crack of a certain size (Fig. 3b).

The state just after initiation (*i.e.*, the first recorded picture for which a crack is observed) is shown for all the studied specimen in Fig.4. Even if the lower and the upper cracks do not initiate at the same exact imposed displacement, the lower and upper part

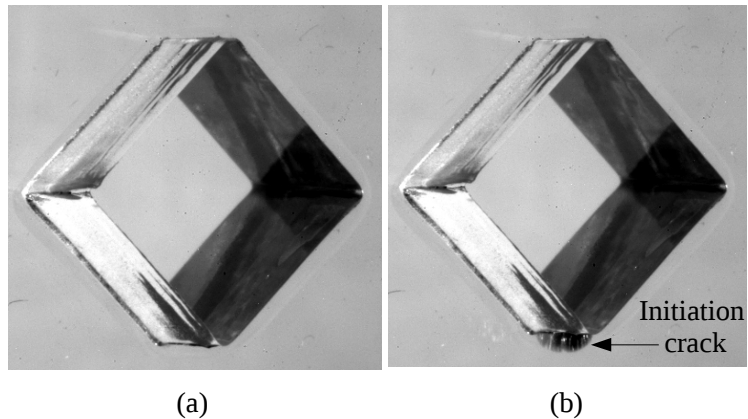


Figure 3: Focus on B3 specimen rhombus hole (6.4mm half-vertical diagonal, 90 deg. angle) (a) just before and (b) at crack initiation highlighting the instantaneous initiation of a crack over a finite size. The imposed displacement variation between both states is 8×10^{-3} mm.

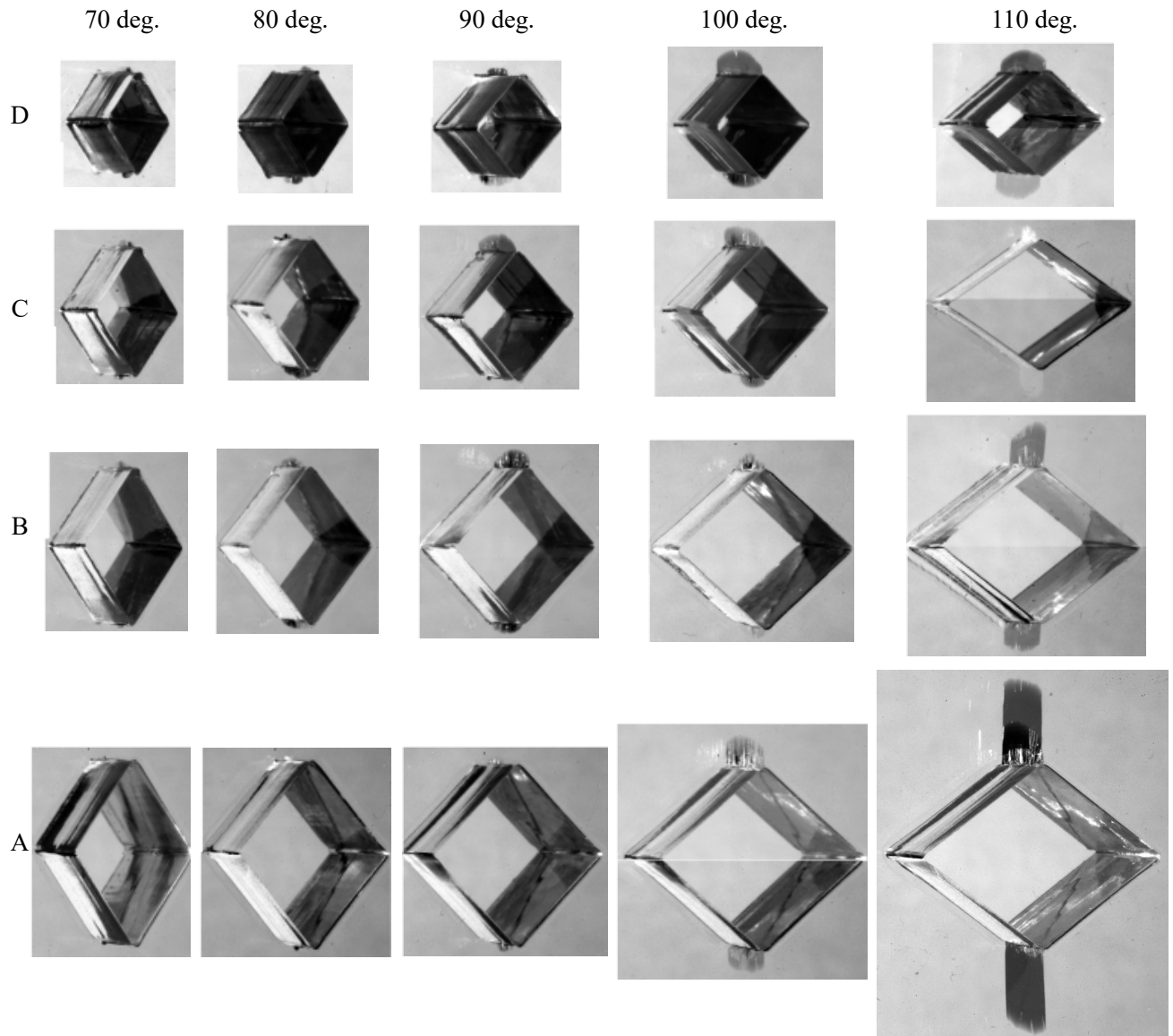


Figure 4: Cracks observed experimentally just after initiation in specimens having different hole sizes (A-D) and angles (70-110 deg.).

of each specimens have been gathered on the same picture for visualization purpose in Fig. 4. The present results show a clear evidence of abrupt initiation of a crack over a finite increment, the crack length in the specimen middle even attaining around 7mm in the case of the specimen containing the biggest rhombus hole with the largest angle (Specimen A5). Although it is possible to model a perfectly instantaneous crack initiation using, *e.g.*, the CC [9], in experiments, "spontaneous" must of course be understood in terms of crack initiation occurring during time and loading increments that are small with respect to the overall test time and imposed loading. For specimens in which spontaneous

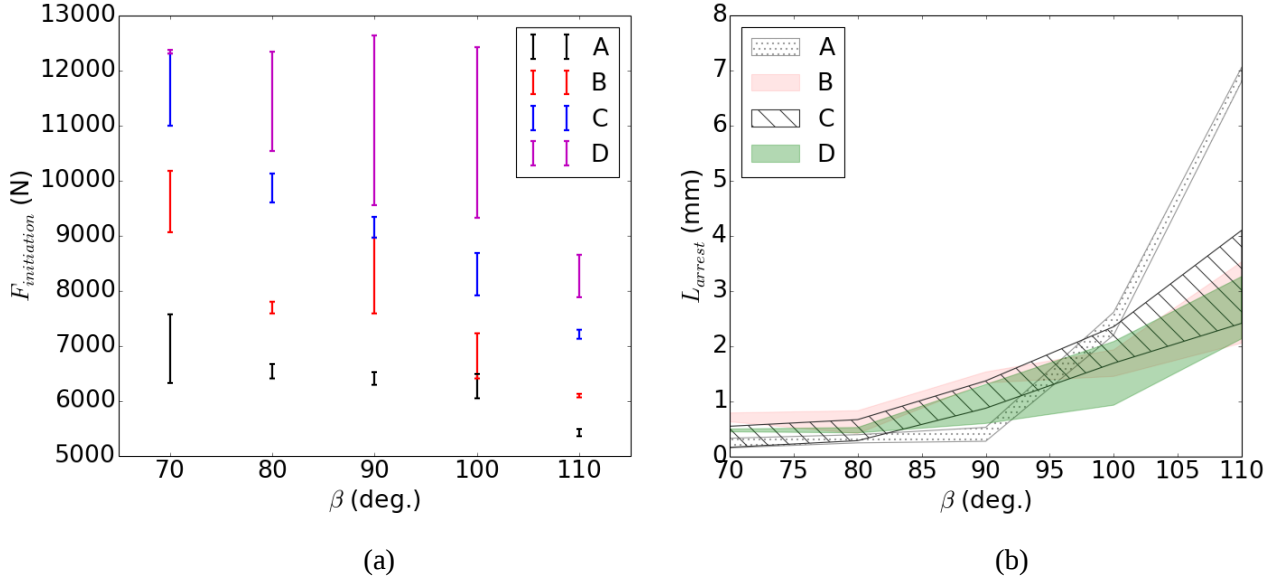


Figure 5: Initiation (a) Force and (b) crack arrest length as a function of the hole angle size (A-D) for specimens with different hole size (A-D).

crack initiation occurs, the crack front shape is rather curved. The crack size just after initiation, that will be referred to as crack arrest length in the following, depends on the rhombus size and angle. The initiation forces and crack arrest lengths (in the specimen middle plane) as a function of the rhombus angle for different hole sizes are shown in Fig. 5. With increasing hole size and angle, the crack size just after initiation tends to increase whereas the initiation force decreases. For each specimen, two values of initiation force and crack arrest length are obtained corresponding to the lower and upper V-notch. For most of the specimens, the initiations of the lower and upper V-notch cracks do not occur at the same exact imposed loading. This might be explained by the specimens not being perfectly symmetric or by the possible presence of some flaws at the V-notch. These features might have a more pronounced influence on the first (lower initiation force value) than on the second (larger initiation force value) crack initiation. Therefore, in the following, the quantitative comparison of experimental measurements with numerical predictions will be held with respect to the larger initiation force values (corresponding to the second initiated crack) obtained experimentally for every specimens.

3. The coupled criterion

3.1. Crack initiation

Under overall quasi-static loading, crack initiation prediction with the CC [9] consists in fulfilling simultaneously an energy and a stress conditions. The energy condition requires that the potential energy change between an undamaged and a damaged state ($\Delta W(S) = W(0) - W(S)$, S being the newly created crack surface) is higher than the energy needed to nucleate the crack $G_c \times S$ (where G_c is the material critical energy release rate). The stress condition states that prior to crack nucleation, the whole area corresponding to the initiation crack must undergo a high enough stress state. For an isotropic homogeneous material, this condition consists in comparing the stress normal to the crack plane σ_{nn} to the material strength σ_c . Under linear elasticity and small deformation framework, the stress and the potential energy are respectively proportional to the applied load and the square of applied load, which allows combining both conditions into a single equation that has to be solved in order to determine the initiation loading level and crack length [6, 9]. The crack initiation loading level corresponds to the lower loading level for which both the stress and the energy conditions are fulfilled. In practice, only one calculation is sufficient in order to compute the stress field and hence the stress criterion whereas the energy criterion requires several calculations to be computed in order to obtain the potential energies corresponding to several crack surfaces.

3.2. Stability of the crack propagation

Crack initiation surface (in 3D, or length in 2D) and loading level can be determined by coupling the stress and the energy conditions. The initiation surface predicted using the CC may also be an arrest surface, depending on the studied material and loading conditions [1, 2, 34]. Otherwise, the CC predicts an unstable propagation of the initiated crack to a bigger surface (called the arrest surface), that may even cause the complete failure of the specimen [3, 4, 12]. The unstable propagation of the initiated crack can be determined by computing the differential energy release rate $G = -\frac{dW}{dS}$, which does not require any additional calculations since the potential energy W as a function of the crack surface S has already been computed so as to determine the initiation configuration. It can be shown that configurations for which the initiation surface also is an arrest surface

correspond to stable crack propagation configurations ($G = G_c$ and $\frac{dG}{dS} < 0$), which means that an increase in the loading is required so that the crack can propagate. In the case of unstable crack propagation ($G > G_c$ or ($G = G_c$ and $\frac{dG}{dS} \geq 0$)) just after initiation, the crack propagates without any increase in the loading at least up to a surface S_{min} verifying $G(S_{min}) = G_c$, which provides a lower bound for crack arrest surface. During this unstable propagation step, the released energy is higher than the energy required for the crack propagation (since $G > G_c$), which allows the crack to propagate further to a surface S_{max} if all this energy excess is consumed in propagation rather than dissipated elsewhere [12, 34]. The surface S_{max} , whose determination is detailed in [2, 6, 34], is an upper bound for crack arrest. In experiments, only a part of the energy excess may be consumed in further crack propagation [12, 35]. Since it is really difficult to quantify the ratio between the energy excess that is dissipated or used for further crack propagation, the crack surface observed experimentally may be compared to the lower and upper bound estimates of the crack surface.

4. Crack initiation modeling

4.1. Finite Element models

The implementation of the CC for crack initiation prediction in PMMA rhombus hole specimens requires both the stress and the energy conditions described in Section 3 to be computed. This is done by FE calculations on undamaged and damaged configurations of rhombus hole specimens, whose dimensions are depicted in Fig. 1a. The FE software used for the whole analysis is Abaqus v6.13. The mechanical properties used for both 2D and 3D calculations are $E = 3000\text{MPa}$ (determined experimentally by tensile test on a specimen with no hole), $\nu = 0.37$, $\sigma_c = 72\text{MPa}$ (properties given by the manufacturer) and $G_c = 250\text{J/m}^2$ (determined by confrontation of numerical and experimental crack advance as a function of the force in the stable propagation part of the test). The symmetric configuration of the specimen allows modeling only one specimen quarter (2D) or eighth (3D). It can be checked numerically that there is no interaction between the upper and the lower crack therefore modeling the initiation of either one or two cracks lead to similar results. A displacement along (Oy) direction is prescribed on the specimen top edge (2D) or face (3D). The stress criterion is computed from a calculation on undamaged specimen

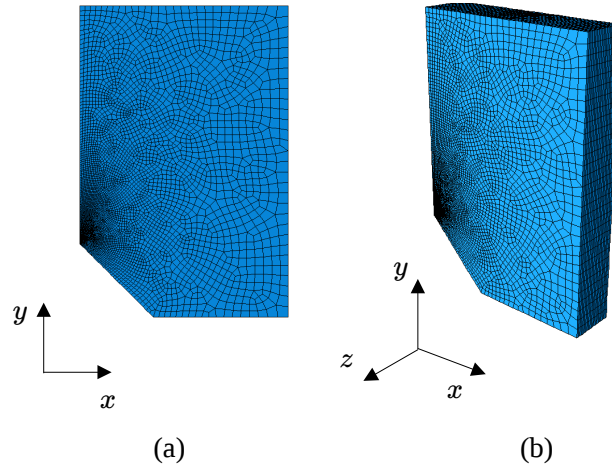


Figure 6: Typical (a) 2D and (b) 3D meshes of one (a) quarter and (b) eighth of the specimen.

meshed with 4 (2D) and 8 (3D) node elements (Fig. 6). As evoked in [6, 21, 22], the initiation length (in 2D) predicted by the coupled criterion usually is a fraction of the material characteristic length $L_{\text{mat}} = \frac{E \times G_c}{\sigma_c^2}$ (in the present analysis, $L_{\text{mat}} \approx 0.145\text{mm}$), which requires fine enough meshes to be correctly captured. A $0.5 \times 10^{-3}\text{mm}$ minimum mesh size is imposed near the V-notch, the mesh being progressively unrefined far from it, which ensures a correct representation of the initiation length or surface as explained in [6].

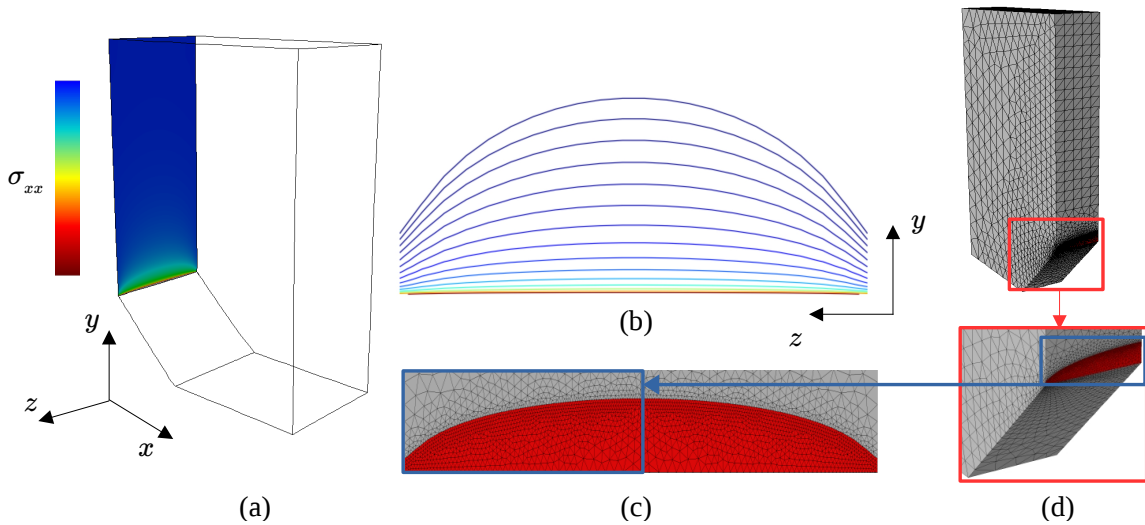


Figure 7: Stress (a) field and (b) isocontours in (Oyz) plane. (c-d) 3D Mesh of one eighth of the specimen including the crack shape determined using a stress isocontour (in (a-c), a symmetry of the stress field and mesh with respect to (Oxy) plane is applied in order to display the whole crack).

The energy criterion is obtained by computing the potential energy of both the undamaged and damaged configuration for several crack lengths or surfaces, which requires the generation of the corresponding crack meshes. In 2D, a crack is only defined by one parameter, namely its length along (Oy)-axis, so that 2D cracked mesh generation is straightforward. Cracked mesh generation is more complex in 3D since the crack shape must be determined *a priori*. Doitrand and Leguillon [3, 4, 5] proposed to determine the 3D possible crack shapes using the stress criterion isocontours. This approach is particularly convenient since a single parameter is sufficient to describe the 3D crack shape, hence limiting the number of calculations to perform to solve the coupled criterion. Moreover, this method ensures a strict fulfillment of the stress criterion over the whole crack surface. Fig. 7a and b shows the normal stress field and isocontours in the crack plane in the undamaged configuration (one quarter of the specimen is shown for visualization purpose), which allows the stress criterion to be computed. It is worth noting that qualitatively, the cracks obtained based on the stress isocontours present a front that has a curved shape, similarly to that observed experimentally (*cf.* Figs. 3 and 4). The same conclusion was drawn by Doitrand and Leguillon [5] concerning the crack shapes obtained based on the stress criterion isocontours under mode I+III loading. Fig. 7c and d show a 3D mesh of one quarter or eighth of the specimen that includes the topology of a crack based on a stress isocontour level. The 3D cracked configurations are meshed with quadratic 10 nodes tetrahedrons in order to avoid meshing difficulties. Since the crack is located in a symmetry plane, it is quite convenient to generate the cracked configuration by removing the symmetry conditions on the crack nodes. The energy criterion is obtained by computing the potential energy change for 15 values of crack surface, each crack shape being based on a stress isocontours. It can be noted that for each cracked configuration, the potential energy of the undamaged and damaged configuration are based on the same mesh topology, the only difference between both cases being the symmetry condition imposed or not on the crack nodes. Using the same mesh topology allows reducing the numerical errors made on the calculation of the potential energy change. Both 2D and 3D approaches have been automatized using python scripts. From a computational point of view, the whole analysis (model generation, calculations and post-treatment) duration takes around 15 minutes in 2D and one hour in 3D.

	Initiation force (N)		Crack arrest length (mm)	
	No sliding	Free sliding	No sliding	Free sliding
Specimen A, $\beta = 70$ deg.	11446	12749	[0.3, 0.5]	[0.4, 0.7]
Specimen D, $\beta = 70$ deg.	17138	20373	[0.05, 0.1]	[0.07, 0.1]
Specimen A, $\beta = 110$ deg.	5883	6053	[6.4, 12.6]	[7.7, 16.5]
Specimen D, $\beta = 110$ deg.	9273	10088	[2.9, 6.6]	[2.9, 6.5]

Table 2: Initiation force and crack arrest length obtained numerically in 2D with either free sliding or no sliding boundary conditions for specimens A and D with $\beta = 70$ deg. or 110 deg. rhombus angle.

4.2. Influence of boundary conditions on crack initiation

The specimen top and bottom faces are in contact with the swivel platens, thus raising the question whether these faces are free or not to slide along x and z direction. The initiation force and crack arrest length lower and upper bounds predicted using the CC with faces free or not to slide are summarized in Table 2 for configurations corresponding to specimens A and D with 70 deg. or 110 deg. rhombus angle. Taking into account or not the top and bottom specimen face sliding has an influence on initiation force. The smaller the specimen hole and hole angle, the lower the differences on the initiation force between no or free sliding boundary conditions (from around 2% for Specimen A5 to 25% for Specimen D1). Experimentally no sliding of the specimen on the swivel platen was observed therefore, in the following, we will consider boundary conditions corresponding to no sliding of the specimen along top and bottom faces.

4.3. Influence of rhombus angle and size on crack initiation

It has been shown in Section 2 that experimentally, crack arrest length and initiation force depend on the rhombus hole size and angle. Following the method explained in Section 3, crack initiation has been computed applying the CC in 2D for the different hole sizes and angles summarized in Tab. 1. Figure 8 shows the obtained initiation forces and crack arrest lengths as a function of the hole angle. The trends of initiation force and crack arrest length as a function of the rhombus angle predicted numerically with the CC are similar to those obtained experimentally. With increasing rhombus angle or hole size, the initiation force decreases whereas the crack arrest length decreases. It can also be noted that the range in crack arrest length is increasing with increasing hole angle.

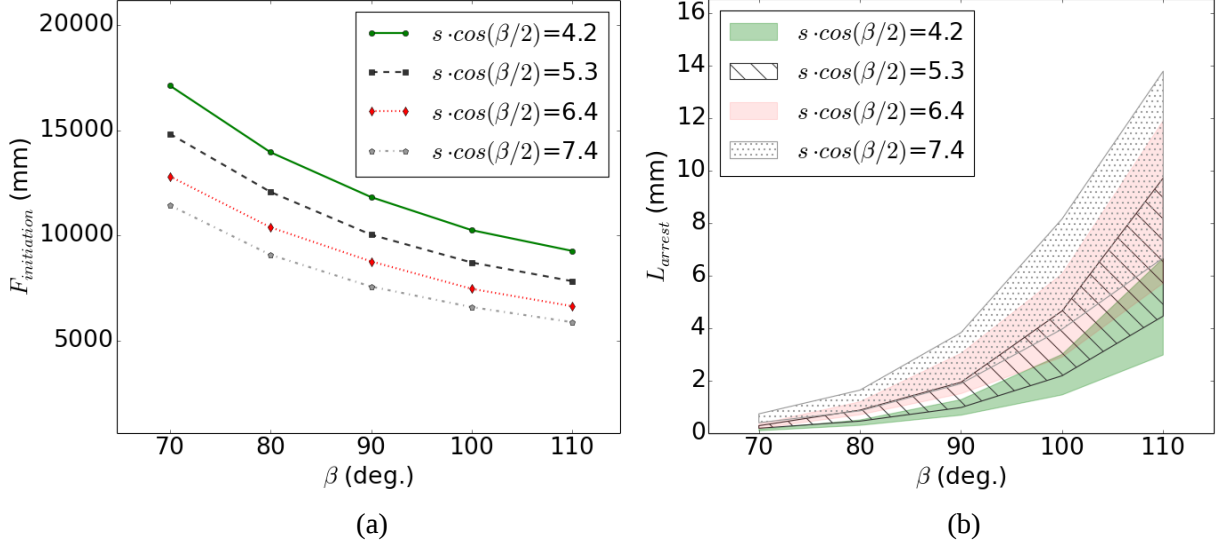


Figure 8: (a) Initiation force and (b) crack arrest length as a function of the rhombus angle β for several hole size.

4.4. Comparison between 2D and 3D models

In the literature, few works concern the comparison between 2D and 3D applications of the CC. Doitrand and Leguillon [4] compared both approaches in the case of crack initiation in scarf adhesive joints under traction and bending. The 3D crack shapes based on the stress isocontours were very close to the extruded 2D crack shapes (i.e, rectangles). Both 2D and 3D predictions led to good qualitative trends compared to experimental results, a slight better quantitative agreement being obtained in 3D. In the present analysis, it is clear from Fig. 7 that 3D crack shapes differ significantly from rectangles and qualitatively look like crack shapes observed experimentally. For instance, for the crack shapes based on the stress isocontours shown in Fig. 7b, the crack length in the specimen middle plane can be around twice as large as its length on the specimen edge. The comparison between 2D and 3D models requires a common parameter describing the crack shape to be determined. A possibility consists in selecting the crack surface, assuming that the 2D calculations are representative of a rectangular crack that would cross the whole specimen. The 3D crack may also be described by its length in the specimen middle plane and compared to the 2D crack length. Fig. 9 shows the 2D and 3D normalized (i) normal stresses $\frac{\sigma_{nn}}{\sigma_c}$ and (ii) incremental energy release rates $\frac{G^{inc}}{G_c}$ (where $G^{inc} = \frac{W(0)-W(S)}{S}$), as a function of either the crack surface (Fig. 9a) or the crack length in the specimen middle plane (Fig. 9b).

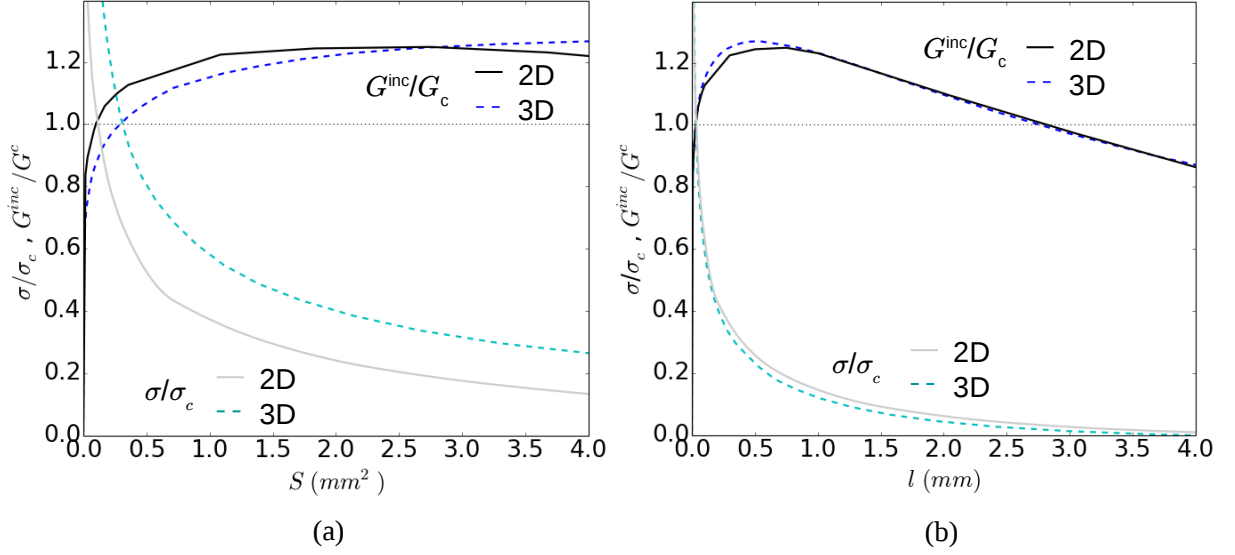


Figure 9: Normalized incremental energy release rates and normal stresses obtained through 2D and 3D FE calculations as a function of (a) the crack surface and (b) the crack length in the specimen middle plane.

Describing 2D and 3D cracks by their surfaces lead to significant differences between the incremental energy release rates and stresses whereas similar evolutions are obtained if the crack length in the specimen middle plane is chosen to describe the crack. In particular, the incremental energy release rate maximum obtained in 3D is correctly represented in 2D only if the crack length corresponds to the 3D crack length in the specimen middle plane. Therefore, 2D modeling seems to provide a good representation of the 3D crack advance in the specimen middle plane. Fig. 10 shows the initiation forces and crack arrest lengths obtained as a function of the rhombus angle for several hole size. The crack arrest lengths predicted either in 2D or 3D are really close to each other, which supports the conclusion that 2D modeling provides an appropriate representation of the 3D crack length in the specimen middle plane. However, crack initiation force is overestimated in 2D compared to the 3D case. Differences between 4% and 15% are obtained between 2D and 3D initiation forces for the studied configurations. It is worth noting that, in the present study, the transparency of the material allows measuring the crack length in the specimen center. However, for non-transparent materials for which the crack length in the specimen middle plane cannot be directly measured, the crack length measured experimentally on the specimen edge may be underestimated compared to that in the specimen middle plane.

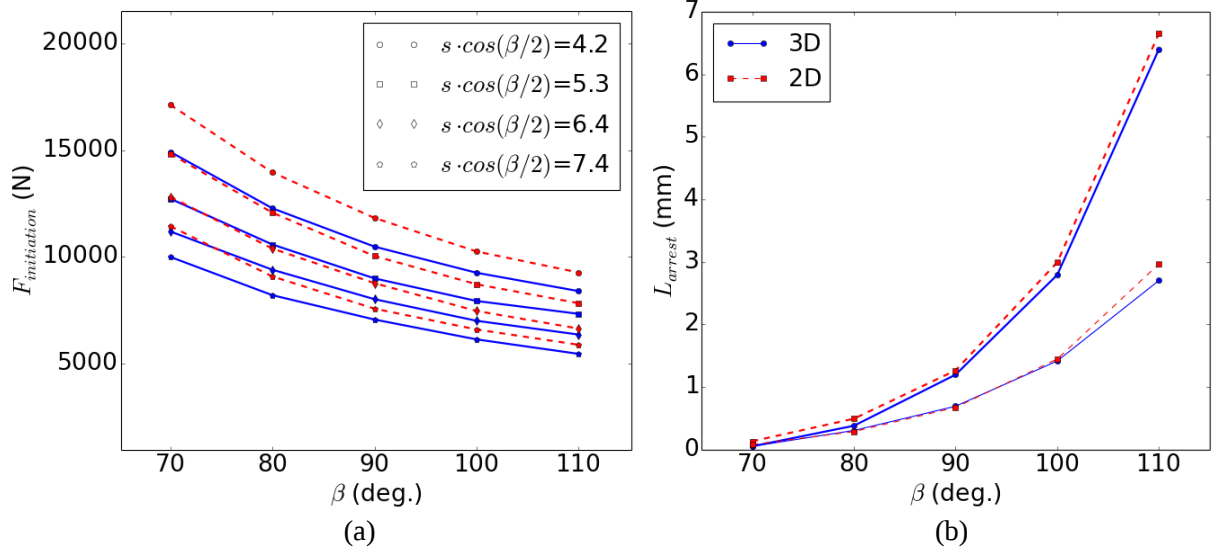


Figure 10: (a) Initiation force and (b) crack arrest length upper and lower bounds as a function of the rhombus angle for (a) several hole size (For visualization purpose, the crack arrest length as a function of the rhombus angle is only displayed for one hole size with half-diagonal $s \times \cos \frac{\beta}{2} = 4.2$ mm).

In this case, special care must be taken when comparing experimental measurement and numerical results, especially if 2D modeling is employed.

5. Comparison between numerical and experimental results

The experimental data measured from the tests presented in Section 2 are compared to the numerical predictions obtained using the CC. Tables 3-6 summarize the initiation forces measured experimentally and obtained through 2D and 3D CC numerical modeling.

~~In Table 3-6, the load corresponding to the appearance of the first crack shows anomalies~~

Initiation force (N)	Specimen A	CC - 2D	CC - 3D
$\beta = 110$ deg.	[5352, 5493]	5883	5457
$\beta = 100$ deg.	[6043, 6481]	6600	6136
$\beta = 90$ deg.	[6295, 6526]	7577	7068
$\beta = 80$ deg.	[6408, 6663]	9088	8246
$\beta = 70$ deg.	[6329, 7756]	11446	10066

Table 3: Initiation force as a function of the specimen rhombus hole angle obtained experimentally and numerically by 2D and 3D FE modeling for specimens A.

Initiation force (N)	Specimens B	CC - 2D	CC - 3D
$\beta = 110$ deg.	[6053, 6118]	6643	6333
$\beta = 100$ deg.	[6396, 7228]	7469	6982
$\beta = 90$ deg.	[7581, 8968]	8774	7954
$\beta = 80$ deg.	[7591, 7806]	10395	9289
$\beta = 70$ deg.	[9057, 10174]	12822	11324

Table 4: Initiation force as a function of the specimen rhombus hole angle obtained experimentally and numerically by 2D and 3D FE modeling for specimens B.

Initiation force (N)	Specimens C	CC - 2D	CC - 3D
$\beta = 110$ deg.	[7126, 7288]	7833	7270
$\beta = 100$ deg.	[7919, 8678]	8722	8003
$\beta = 90$ deg.	[8969, 9347]	10045	9033
$\beta = 80$ deg.	[9595, 10127]	12079	10628
$\beta = 70$ deg.	[11001, 12308]	14842	12886

Table 5: Initiation force as a function of the specimen rhombus hole angle obtained experimentally and numerically by 2D and 3D FE modeling for specimens C.

Initiation force (N)	Specimens D	CC - 2D	CC - 3D
$\beta = 110$ deg.	[7887, 8652]	9273	8433
$\beta = 100$ deg.	[9331, 12420]	10261	9222
$\beta = 90$ deg.	[9557, 12631]	11833	10517
$\beta = 80$ deg.	[10541, 12339]	13966	12334
$\beta = 70$ deg.	[12312, 12379]	17138	15059

Table 6: Initiation force as a function of the specimen rhombus hole angle obtained experimentally and numerically by 2D and 3D FE modeling for specimens D.

~~for some small angle configurations. As already mentionned they are likely due to a bigger sensitivity to defects in these specimens. Fig. 11 presents the initiation force variation as a function of the rhombus angle measured experimentally and obtained numerically in 3D. The initiation forces measured for specimens in which crack initiation is influenced by a flaw (cf. Fig. 2 and Table 3 for instance) are lower than that predicted by the CC.~~

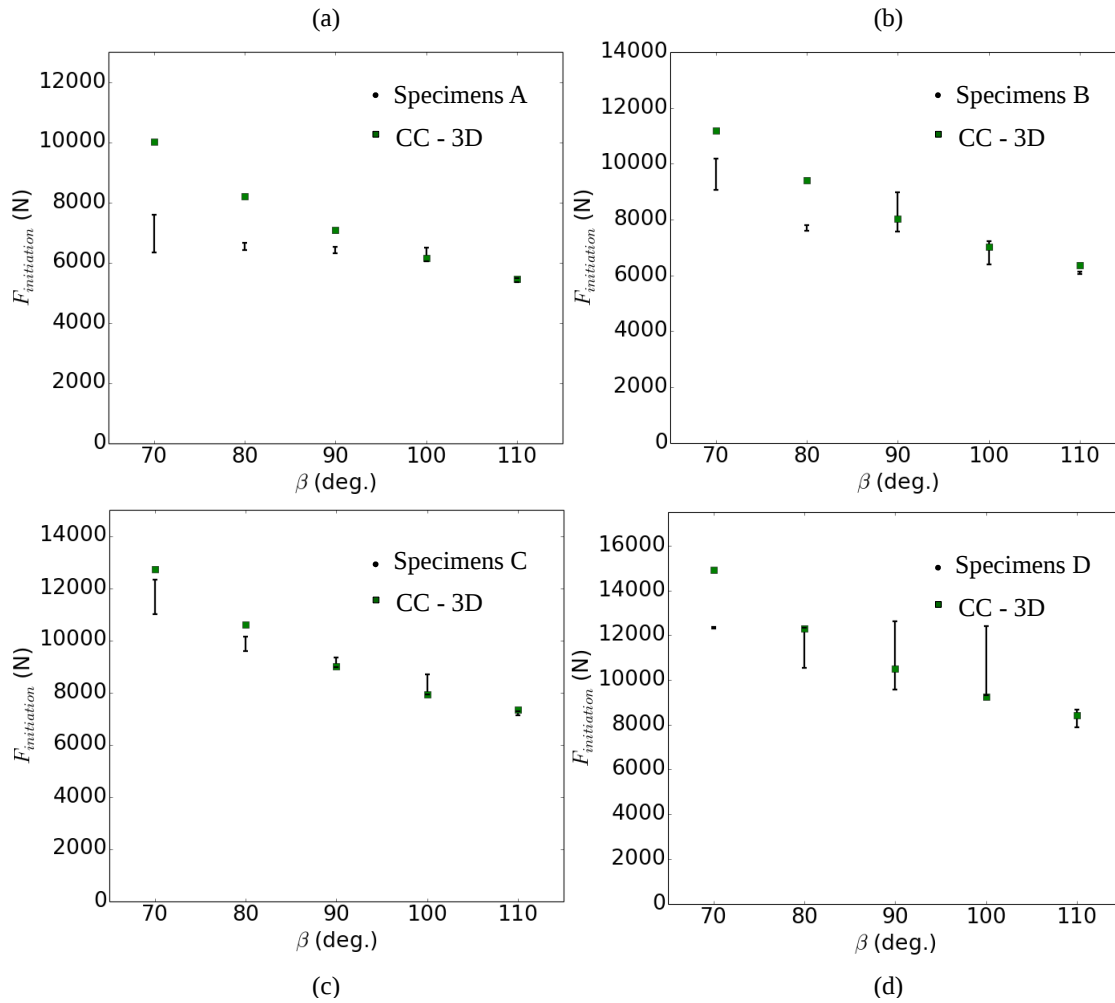


Figure 11: Initiation forces (i) measured experimentally and (ii) obtained numerically using the CC (in 3D) as a function of the rhombus hole angles of specimens (a) A, (b) B, (c) C and (d) D.

~~Since in the model, the influence of possible flaws was not taken into account differences up to 30% (3D) and 50% (2D) on initiation forces are obtained for these configurations.~~

However, for specimens in which a spontaneous crack initiation was observed, a reasonable agreement between numerical predictions and experimental measurements is obtained. Fig. 12 shows the crack arrest lengths as a function of the specimen rhombus angle for the four studied rhombus hole sizes. It seems that the crack arrest upper bound predicted by the CC overestimates the crack lengths measured experimentally. However, similar orders of magnitude are obtained between the crack arrest length measured experimentally and the crack arrest lower bound predicted by the usual arrest criterion $G = G_c$ and $\frac{dG}{dS} < 0$ (*cf.* Section 3).

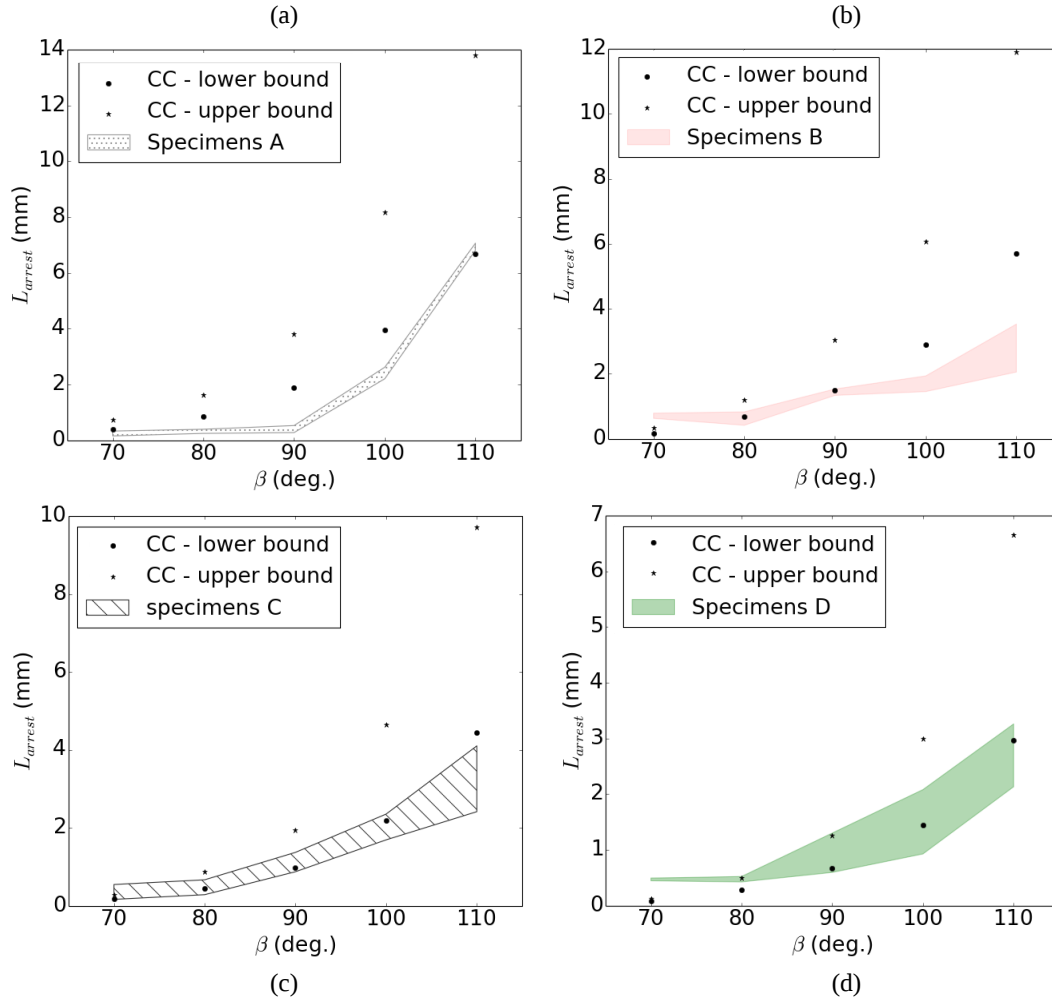


Figure 12: Crack arrest lengths (i) measured experimentally and (ii) lower and upper bounds obtained numerically using the CC as a function of the rhombus hole angles of specimens (a) A, (b) B, (c) C and (d) D.

6. Conclusion

The experimental characterization of crack initiation in PMMA rhombus hole specimens allows supporting a major hypothesis assumed when modeling crack initiation with the coupled criterion: Spontaneous crack initiation is observed experimentally in specimens that do not contain major flaws around the V-notch, which means that a crack nucleates and propagates in an unstable manner over a finite size in a really short time and displacement increments. Since crack nucleation followed by unstable propagation to an arrest length occurs quasi-instantaneously, both phases (initiation and unstable propagation) cannot be distinguished experimentally as easily as in numerical models. Both the

initiation force and crack size depend on the rhombus hole size and angle. With increasing hole size and angle, the crack size just after initiation increases whereas the initiation force decreases. For all the tested specimens, the crack front shape is curved. A rather progressive crack growth is observed in the case of specimens containing a flaw around the V-notch.

The same initiation force and crack length trends as obtained experimentally depending on the rhombus hole size and angle are qualitatively well captured by 2D and 3D FE modeling of crack initiation using the coupled criterion. These quantities depend both on the specimen geometry and on boundary conditions. Compared to the 3D case, modeling the problem in 2D provides a good estimate of the crack evolution in the specimen middle plane. Indeed, the 2D and 3D incremental energy release rates as a function of the crack surface show significant differences whereas similar evolutions are obtained as a function of the 2D crack length or the 3D crack length in the specimen middle plane. Moreover, the crack arrest lengths obtained in 2D and 3D (considering the crack length in the specimen middle plane) are really close to each other. The main difference between 2D and 3D results lies in the predicted initiation force, which is overestimated by up to 15% in 2D compared to 3D results for the studied configurations. Compared to experimental data, the initiation force predicted using the CC is clearly overestimated for specimens for which a crack nucleated around a flaw. However, similar order of magnitude are obtained for the specimens for which a spontaneous crack initiation was observed. The predicted crack arrest length lower bounds are also in the same order of magnitude as those measured experimentally.

Rhombus hole specimens are quite convenient to study crack initiation since the stress singularity created by the V-notch allows considering only a linear elastic behavior of the material. If circular hole specimens are considered, no singularity emanates from the hole and larger imposed loading are necessary, which may probably require to take into account the material nonlinear behavior. This is an interesting perspective since up to now, only few application of the coupled criterion including material or geometrical nonlinearities [31, 33] exist.

References

- [1] Doitrand, A., Fagiano, C., Carrère, N., Chiaruttini, V., Hirsekorn, M., 2017. Damage onset modeling in woven composites based on a coupled stress and energy criterion. *Engng. Fract. Mech.* 169, 189-200.
- [2] Doitrand, A., Fagiano, C., Hild F., Chiaruttini, V., Mavel A., Hirsekorn, M., 2017. Mesoscale analysis of damage growth in woven composites *Compos Part A.* 96, 77-88.
- [3] Doitrand, A., Leguillon, D, 2018. 3D application of the coupled criterion to crack initiation prediction in epoxy/aluminum specimens under four point bending. *Int. J. Sol. Struct* 143, 175-182.
- [4] Doitrand, A., Leguillon, D, 2018. Comparison between 2D and 3D applications of the coupled criterion to crack initiation prediction in scarf adhesive joints. *Int. J. Adh. Adh.* 85, 69-76.
- [5] Doitrand, A., Leguillon, D, 2018. Numerical modeling of the nucleation of facets ahead of a primary crack under modeI+III. *Int. J. Fract.*, doi:10.1007/s10704-018-0305-8.
- [6] Doitrand, A., Estevez, R.,Leguillon, D. Comparison between cohesive zone and coupled criterion modeling of crack initiation in rhombus hole specimens under quasi-static compression. Submitted to *Theor. App. Fract. Mech.*
- [7] García, I.G., Carter, B.J., Ingraffea, A.R., Mantič V., 2016. A numerical study of transverse cracking in cross-ply laminates by 3D finite fracture mechanics. *Compos. Part B* 95, 475-487.
- [8] Hashin, Z.,1996. Finite thermoelastic fracture criterion with application to laminate cracking analysis. *J. Mech. Phys. Solids* 44(7), 1129-1145.
- [9] Leguillon, D., 2002. Strength or toughness? A criterion for crack onset at a notch. *Eur. J. Mech. - A/Solids* 21 (1), 61-72.
- [10] Leguillon D., Yosibash Z., 2003. Crack onset at a v-notch. Influence of the notch tip radius. *Int. J. Fract.* 122(1-2), 1-21.

- [11] Leguillon, D. , Quesada, D. , Putot, C. , Martin, E. , 2007. Size effects for crack initiation at blunt notches or cavities. *Engng. Fract. Mech.* 74, 24202436 .
- [12] Leguillon, D., Martin E., 2013. The strengthening effect caused by an elastic contrast Part I: the bimaterial case. *Int. J. Fract.* 179, 157-167.
- [13] Leguillon, D., 2014. An attempt to extend the 2D coupled criterion for crack nucleation in brittle materials to the 3D case. *Theor. Appl. Fract. Mech.* 74, 7-17.
- [14] Leguillon D., Martin E., Seveček O., Bermejo R. (2015). Application of the coupled stress-energy criterion to predict the fracture behaviour of layered ceramics designed with internal compressive stresses. *Eur. J. Mech. A/Solids* 54, 94-104.
- [15] Leguillon D., Yosibash Z., 2017. Failure initiation at V-notch tips in quasi-brittle materials. *Int. J. Solids Structures*, 122-123, 1-13.
- [16] Leguillon D., Martin E., Seveček O., Bermejo R, 2018. What is the tensile strength of a ceramic to be used in numerical models for predicting crack initiation? *Int. J. Fract.* 212(1), 89-103.
- [17] Li J., Leguillon N D., 2018. Finite element implementation of the coupled criterion for numerical simulations of crack initiation and propagation in brittle or quasi-brittle materials. *Theor. Appl. Fract. Mech.*, 93, 105-115.
- [18] Mantič, V., 2009. Interface crack onset at a circular cylindrical inclusion under a remote transverse tension. Application of a coupled stress and energy criterion. *Int. J. Sol. Struct.* 46, 1287-1304.
- [19] Mantič, V., García, I.G., 2012. Crack onset and growth at the fibre-matrix interface under a remote biaxial transverse load. Application of a coupled stress and energy criterion. *Int. J. Solids Structures* 49, 2273-2290.
- [20] Martin, E., Leguillon, D., 2004. Energetic conditions for interfacial failure in the vicinity of a matrix crack in brittle matrix composites. *Int. J. Solids Structures* 41, 6937-6948.

- [21] Martin, E., Leguillon, D., Carrère, N., 2012. A coupled strength and toughness criterion for the prediction of the open hole tensile strength of a composite plate. *Int. J. Solids and Structures* 49 (26), 3915-3922.
- [22] Martin, E., Leguillon, D., Seveček, O., Bermejo, R., 2018. Understanding the tensile strength of ceramics in the presence of small critical flaws. *Engng. Fract. Mech.* doi:10.1016/j.engfracmech.2018.06.021.
- [23] Mittelman, B., Yosibash, Z., 2014. Asymptotic analysis of the potential energy difference because of a crack at a V-notch edge in a 3D domain. *Engng. Fract. Mech.* 131, 232-256.
- [24] Mittelman, B., Yosibash, Z., 2015. Energy release rate cannot predict crack initiation orientation in domains with a sharp V-notch under mode III loading. *Engng. Fract. Mech.* 141, 230-241.
- [25] Nairn, J.A., 2000. Exact and variational theorems for fracture mechanics of composites with residual stresses, traction-loaded cracks and imperfect interfaces. *Int J Fract* 105:243271.
- [26] Yosibash, Z., Mittelman, B., 2016. A 3-D failure initiation criterion from a sharp V-notch edge in elastic brittle structures. *Eur. J. Mech. A/Solids* 60, 70-94.
- [27] Pham K.H., Ravi-Chandar K., 2016. On the growth of cracks under mixed-mode I+III loading. *Int. J. Fract.* 199, 105-134.
- [28] Picard D., Leguillon D., Putot D, 2006. A method to estimate the influence of the notch-root radius on the fracture toughness measurement of ceramics. *J. Eur. Cer. Soc.* 26(8), 1421-1427.
- [29] Reinoso, J. , Arteiro, A. , Paggi, M. , Camanho, P.P. , 2017. Strength prediction of notched thin ply laminates using finite fracture mechanics and the phase field approach. *Compos. Sci. Technol.* 150, 205-216.
- [30] Romani R., Bornert M., Leguillon D., Le Roy R., Sab K., 2015. Detection of crack onset in double cleavage drilled specimens of plaster under compression by digital

image correlation - Theoretical predictions based on a coupled criterion. Eur. J. Mech. A/Solids 51, 172-182.

- [31] Rosendahl, P.L., Staudt, Y., Odenbreit, C., Schneider, J., Becker, W., 2017. Silicone sealants : a finite fracture mechanics failure model for non-linear materials. 14th International Conference on Fracture (ICF14), June 18-23, 2017 ,Rhodes, Greece.
- [32] Stein N., Weigraeber P., Becker W., 2015. A model for brittle failure in adhesive lap joints of arbitrary joint configuration. Compos Struct 133, 707-718.
- [33] Talmon l'Armée, A., Hell, S., Rosendahl, P.L., Felger, J., 2017. Nonlinear crack opening integral : Mode mixity for finite cracks. Engng. Fract. Mech. 186, 283-299.
- [34] Weißgraeber, P., Leguillon, D., Becker, W., 2016. A review of Finite Fracture Mechanics: crack initiation at singular and non-singular stress raisers. Archive Appl. Mech. 86 (1-2), 375401.
- [35] Weissgraeber P, Hell S, Becker W, 2016. Crack nucleation in negative geometries. Engng. Fract. Mech. 168, 93-104.